

Laser writing of coherent colour centres in diamond

Yu-Chen Chen¹, Patrick S. Salter², Sebastian Knauer³, Laiyi Weng¹, Angelo C. Frangescou⁴, Colin J. Stephen⁴, Shazeaa N. Ishmael⁴, Philip R. Dolan¹, Sam Johnson¹, Ben L. Green⁴, Gavin W. Morley⁴, Mark E. Newton⁴, John G. Rarity³, Martin J. Booth² and Jason M. Smith^{1*}

Optically active point defects in crystals have gained widespread attention as photonic systems that could be applied in quantum information technologies^{1,2}. However, challenges remain in the placing of individual defects at desired locations, an essential element of device fabrication. Here we report the controlled generation of single negatively charged nitrogen-vacancy (NV⁻) centres in diamond using laser writing³. Aberration correction in the writing optics allows precise positioning of the vacancies within the diamond crystal, and subsequent annealing produces single NV⁻ centres with a probability of success of up to 45 ± 15%, located within about 200 nm of the desired position in the transverse plane. Selected NV⁻ centres display stable, coherent optical transitions at cryogenic temperatures, a prerequisite for the creation of distributed quantum networks of solid-state qubits. The results illustrate the potential of laser writing as a new tool for defect engineering in quantum technologies, and extend laser processing to the single-defect domain.

The NV⁻ colour centre is one of an increasing number of point defects in wide bandgap materials such as diamond and silicon carbide that show promise as quantum light sources and provide an optical interface with coherent electronic and nuclear spins^{4–11}. The realization of entangled networks for sensing or distributed quantum computing with these systems^{12,13} requires coherence of the optical transition, which some defects have displayed at cryogenic temperatures^{7,14}. With NV⁻ centres this coherent interface has been used to demonstrate spin–photon entanglement¹⁵ and entanglement between distant spins¹⁶.

To realize technological applications it will be necessary to integrate such colour centres with optical and electronic components by positioning them at desired locations^{17–20} with an accuracy of 10 nm–1 µm. This presents a challenge, as most placement methodologies involve irradiation of the sample with electrons or ions, creating residual damage to the crystal lattice and degrading the properties of the colour centre. Despite recent progress using advanced annealing recipes and low-energy electron beams^{21,22}, new methods for the placement of defects with minimal residual lattice damage are of considerable interest.

Here we show that laser writing can be employed to generate vacancies in a crystal as a starting point for the formation of coherent colour centres. This method has several attractive features: the highly nonlinear process of laser writing³ combined with appropriate aberration correction²³ permits vacancy generation with a spatial resolution beyond the optical diffraction limit, at any depth in the diamond, without damaging the overlaying material and the laser pulse energy can be tuned with high precision to control the

number of vacancies generated. We show that after applying this process to diamond samples in which nitrogen atoms are present at low concentrations, subsequent annealing produces single, high-quality NV⁻ centres near the target locations.

The diamond samples were commercially available single crystals grown by chemical vapour deposition, with nitrogen density below 5 ppb (900 atoms per µm³). The regions chosen for processing contained no ‘native’ NV centres. Single writing pulses of wavelength 790 nm and duration 300 fs were delivered to each site in 25 × 20 square grids with a pitch of 5 µm at a depth of 50 µm. Along one axis of the grids, the pulse energy E_p was varied between 16.0 nJ and 61.8 nJ to generate incremental degrees of damage to the lattice. Along the other axis, 20 identical pulses were delivered to facilitate statistical analysis of the results for each pulse energy. The onset of lattice damage at low pulse energies is thought to occur by a nine-photon ionization process²⁴ (see Supplementary Information), from which we estimate the resolution of vacancy writing to be 120 nm in the image plane and 500 nm in the axial direction (see Methods).

Figure 1a shows a photoluminescence (PL) image of a grid immediately after laser writing. E_p increases from the bottom to the top of the image. Visible fluorescence was produced from sites that had been exposed to pulses with $E_p > 31$ nJ (red line), and the PL spectra (Fig. 1b, lower trace) confirmed the presence of photo-generated neutral vacancies (GR1 centres). We estimate that around 10^7 vacancies are generated by the pulse energy E_1 (see Methods).

Figure 1c shows the PL image of the same grid after annealing (see Methods). Fluorescence was observed at several sites for which $E_p < E_1$, indicating the formation of new colour centres. Spectroscopy revealed that all fluorescence from sites up to $E_2 = 36.4$ nJ (green line) was from NV⁻ centres, with a characteristic zero phonon line (ZPL) at 637 nm and a broad phonon sideband (Fig. 1b, middle spectrum). GR1 fluorescence was no longer observed, suggesting that the majority of the vacancies had been removed as a result of the annealing step²⁵. Neutral NV centre (NV⁰) ZPL signatures at 575 nm were also absent, further signifying a low vacancy concentration (see Supplementary Information). Features created with $E_p > E_2$ showed broadband fluorescence (Fig. 1b upper trace), suggesting that the damage created at these sites exceeded the threshold for graphitization during the annealing²⁶.

Photon autocorrelation measurements (see Methods) were carried out for each of the sites with $E_p < E_1$ to determine the number of NV⁻ centres present. Figure 2a shows a typical data set revealing a dip at $\delta t = 0$, characteristic of a single colour centre.

¹Department of Materials, University of Oxford, Parks Road, Oxford OX1 3PH, UK. ²Department of Engineering Science, University of Oxford, Parks Road, Oxford OX1 3PJ, UK. ³Department of Electronics and Electrical Engineering, University of Bristol, Merchant Venturers Building, Woodland Road, Bristol BS8 1UB, UK. ⁴Department of Physics, University of Warwick, Coventry CV4 7AL, UK. *e-mail: jason.smith@materials.ox.ac.uk

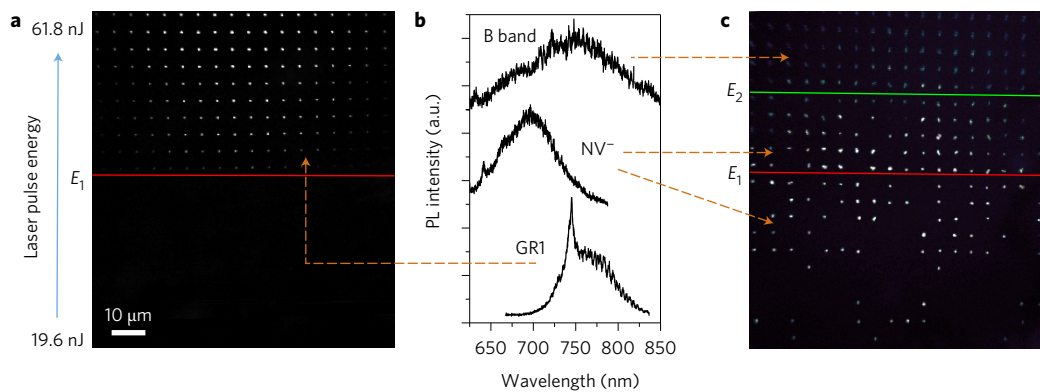


Figure 1 | Generation of NV[−] colour centres using laser processing. **a**, PL image of the 25 × 20 array immediately after laser processing (before annealing). The laser pulse energy increases from the bottom to the top of the image. The red line at pulse energy E_1 indicates the lowest energy laser pulse that produces visible fluorescence. The drop-off in intensity of features towards the edge of the array is due to field aberrations in the PL microscope. **b**, Typical spectra measured from points in **a** that are characteristic of GR1 (single-vacancy) defects, and from **c** below energy E_2 (characteristic of the NV[−] centre) and above energy E_2 (characteristic of the radiation B band), as indicated by the orange arrows. **c**, PL image of the same region of the sample after the annealing process, showing NV[−] emission from multiple sites processed with pulse energies both above and below E_1 . The green line at pulse energy E_2 indicates the graphitization threshold.

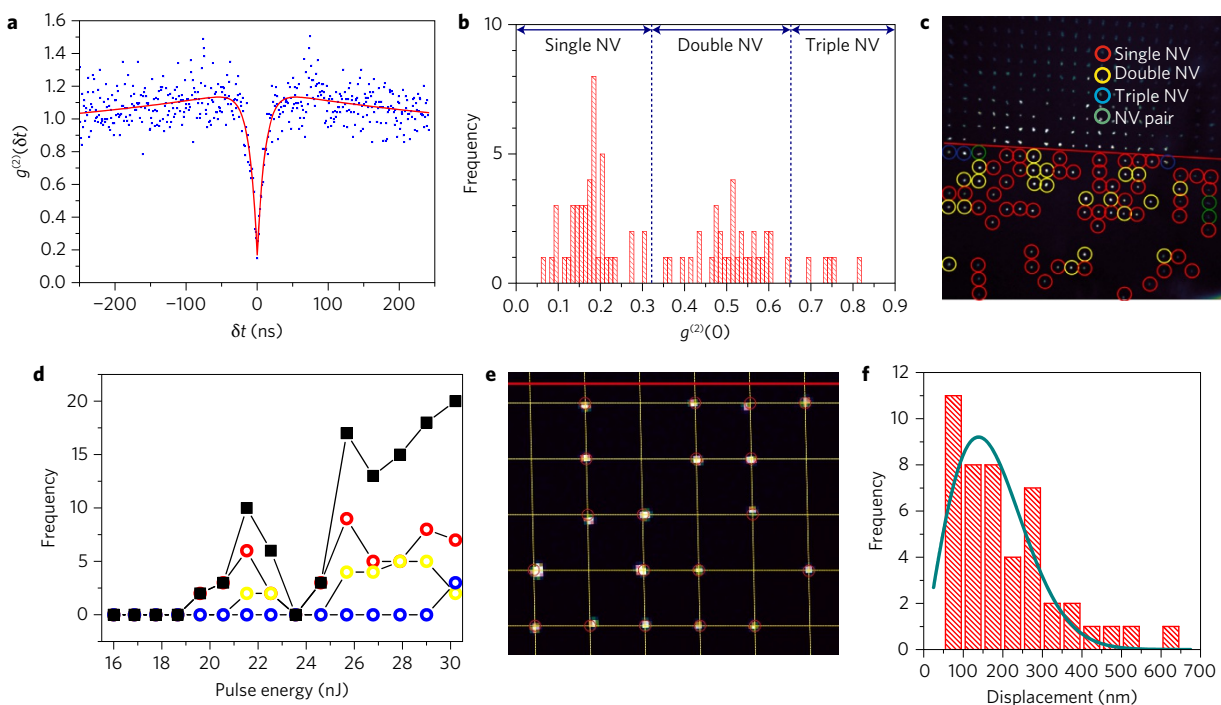


Figure 2 | Statistics and positioning accuracy of NV generation using laser processing. **a**, Histogram showing $g^{(2)}(\delta t)$ from a single NV centre. **b**, Histogram of $g^{(2)}(0)$ for the different laser processing sites, allowing the identification of sites of single, double and triple NV centre generation. **c**, Map of the number of NV centres generated at different sites. ‘NV pair’ refers to a double NV where the two defects are spatially resolved. **d**, Plot of the number of single (red), double or pair (yellow) and triple (blue) NV centres generated in each row of 20 sites as a function of laser pulse energy measured before the objective lens in the writing apparatus. The total number generated per row is shown in black. **e**, Magnified image of NV centre fluorescence relative to the laser processing grid. Red circles centred on the grid points are 1 μm in diameter. **f**, Histogram of the displacement in the image plane for the single NV centres measured after correction for field distortion in the PL microscope. The data are fitted with a cylindrical distribution function (see text).

A histogram of $g^{(2)}(0)$ values from all sites measured is shown in Fig. 2b. Two populations emerge, one with $g^{(2)}(0) < 0.32$ and another with $0.32 < g^{(2)}(0) < 0.65$, which we attribute to the presence of one- and two-colour centres, respectively. A few sites showed $g^{(2)}(0)$ values between 0.65 and 0.9, which we attribute to the presence of three-colour centres. Figure 2c shows a spatial map of the NV[−] populations per site, and Fig. 2d shows the row statistics versus the writing pulse energy. At $E_p = 25.7$ nJ, 9 out of 20 sites revealed a single NV[−], which corresponds to a probability of

$45 \pm 15\%$, consistent with the statistical optimum of 37%. The total number of NV centres per row (black squares) reveals a systematic trend for more to be generated at higher pulse energies, but with a region of deviation from this trend spanning five rows, attributable to non-uniform nitrogen distribution in the sample.

From the PL image the location of each NV[−] in the image plane can be determined to within <100 nm. Figure 2e shows a magnified image of a section of the NV[−] array with a superimposed grid showing the nominal target positions. A histogram of the measured

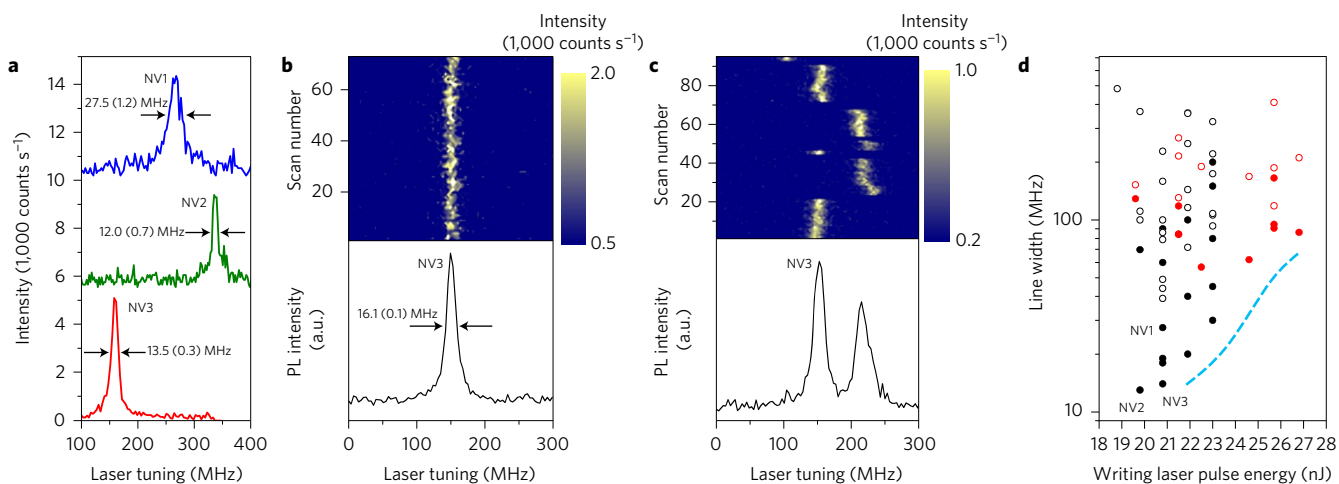


Figure 3 | Spectral properties of single laser-generated NV centres at 4.2 K. **a**, PLE (single sweep) of three different NV centres, with two showing Lorentzian peaks below 14 MHz in width. FWHM values from Lorentzian peak fits are given, with errors in parentheses. **b**, Colourscale map of repeated PLE spectra of NV3, showing a stable line over 70 laser sweeps with an inhomogeneous linewidth of 16.1 MHz. **c**, Spectral jumping as a result of a 532 nm re-pump pulse required to restore the negative charge state on ionization. The lower plots in **b** and **c** are aggregates of the consecutive sweeps in the colourscale images. **d**, Scatter plot of the single-scan linewidth (solid circles) and re-pump-broadened linewidth (open circles) for different energies of the laser writing pulse. Data from samples A and B are shown as red and black circles, respectively. The dashed blue line is a guide showing a trend to larger single-scan linewidths with higher pulse energies (see main text).

displacements of the NV^- centres from the target points (see Methods) is shown in Fig. 2f. The displacements measured are significantly larger than the predicted radial distribution of laser-generated vacancies, suggesting that the diffusion of vacancies during the anneal stage determines the spatial distribution of the NV centres. The solid line is a fit of the two-dimensional (2D) distribution function $f(r) = A r e^{-r^2/r_0^2}$ where r is the radial displacement and A and r_0 are fitting parameters (see Methods). r_0 was found to be 196 ± 20 nm, consistent with the expected thermal diffusion length (see Supplementary Information). On the basis of this distribution, 61% of the NV centres fall within r_0 of the target position in the image plane. In the axial direction the positioning accuracy is expected to be lower, around 700 nm, due to the elongated shape of the vacancy generation volume (see Methods).

PL excitation (PLE) spectroscopy (see Methods) was used to probe the ZPLs of the NV^- centres at temperature $T = 4.2$ K, and reveals examples of colour centres with highly coherent transitions. Figure 3a shows a selection of PLE scans from three NV⁻ centres, revealing widths of 13.5 ± 0.3 MHz, 12.0 ± 0.7 MHz and 27.5 ± 1.2 MHz. The two narrowest lines are consistent with the Fourier transform limit of 12.4 ± 0.1 MHz for an NV⁻ centre in bulk diamond

based on a fluorescence relaxation time of 12.8 ± 0.1 ns (see Supplementary Information). Of the 50 NV⁻ centres measured, 25 showed clear PLE signals, seven with linewidths below 30 MHz and four under 20 MHz. Repeated scans of one of these colour centres (Fig. 3b) revealed only small fluctuations in the peak position, producing an inhomogeneously broadened line of width 16.1 MHz. After prolonged (~ 30 s) excitation the NV⁻ centre ionized to NV⁰ and an optical repump was required to restore the negative charge state. The repump pulse ionized other defects in the vicinity of the NV centre, changing the local electric field and shifting its transition energy by about 70 MHz via the Stark effect (Fig. 3c). Such shifts can be suppressed by using a repump tuned to 575 nm^{21,27}, or corrected using dynamic stabilization techniques²⁸.

Figure 3d shows the measured single-scan linewidths (solid circles) and repump-broadened linewidths (open circles) for the NV⁻ centres measured from two samples (A and B), plotted against the energy of the laser writing pulse used. Although a wide range of linewidths is observed for each pulse energy setting and the narrowest linewidths displayed in sample A are around 60 MHz, the narrowest linewidth identified across both samples increases systematically with increasing pulse energy (indicated by the blue dashed lines), suggesting that residual damage may limit the homogeneous linewidth at progressively higher pulse energies. Birefringence and Raman scattering measurements revealed evidence of residual stress only at sites that correspond to pulse energies well above E_2 (see Supplementary Information).

Finally, we measured the electron spin properties of the written NV⁻ using optically detected magnetic resonance. Hahn echo measurements (see Methods) showed decoherence (T_2) times typically between 30 and 80 μ s (Fig. 4a), while one NV⁻ centre showed $T_2 > 100$ μ s. Such coherence times are comparable to those reported for NV⁻ centres implanted in a similar diamond material using ion beam methods²⁹. No correlation was observed between the optical linewidth and spin coherence, although it is worth noting that the NV⁻ centre with the longest T_2 value also showed a narrow ZPL width of 27.5 MHz (NV1 in Fig. 3).

In summary, we show that femtosecond laser writing of vacancies into diamond can be used to produce optically coherent NV⁻ colour centres at desired locations. The submicrometre positioning accuracy achieved is sufficient for placing NV⁻ centres in

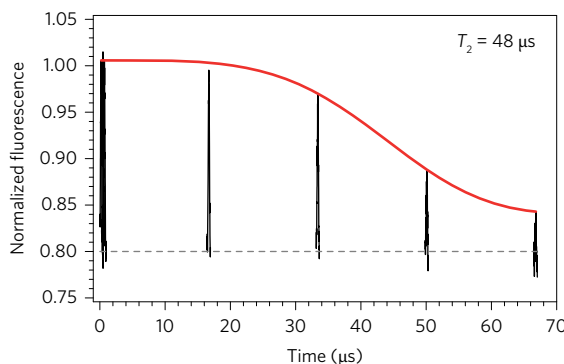


Figure 4 | Spin resonance properties of laser-generated NV centres at 300 K. Hahn echo data for an NV centre created with pulse energy of 19.6 nJ, fitted with the function $I(\tau) = y_1 e^{-(\tau/T_2)^n} + y_0$, where the exponent n is a free parameter and y_0 , y_1 and T_2 are fitting parameters.

optical structures such as multimode waveguides and whispering gallery resonators¹⁸ or under solid immersion lenses¹⁶. The demonstrated accuracy is limited by the diffusion of the vacancies during annealing, and further improvements may be achieved using a higher nitrogen concentration in the starting material and an adjusted annealing recipe. In particular, high-precision depth positioning may be achieved by combining laser writing of vacancies with delta doping of a thin layer of nitrogen-rich material during growth³⁰. The adaptive optics used for aberration correction would also allow colour centres to be positioned under microstructured surfaces. Beyond quantum photonic devices, the ability to write large and detailed 2D or 3D arrays of NV⁻ defects may find application in magnetic-field imaging systems³¹. The laser writing technique demonstrated here for NV centres could be readily applied in conjunction with the writing of subsurface waveguides^{32,33} and electrodes³⁴, and can be adapted for the generation of other colour centres and point defects in other wide bandgap materials.

Methods

Methods and any associated references are available in the [online version of the paper](#).

Received 15 June 2016; accepted 26 October 2016;
published online 5 December 2016

References

1. Weber, J. R. *et al.* Quantum computing with defects. *Proc. Natl Acad. Sci. USA* **107**, 8513–8518 (2010).
2. Dzurak, A. Quantum computing: diamond and silicon converge. *Nature* **479**, 47–48 (2011).
3. Gattass, R. R. & Mazur, E. Femtosecond laser micromachining in transparent materials. *Nat. Photon.* **2**, 219–225 (2008).
4. Jelezko, F., Gaebel, T., Popa, I., Gruber, A. & Wrachtrup, J. Observation of coherent oscillations in a single electron spin. *Phys. Rev. Lett.* **92**, 076401 (2004).
5. Riedel, D. *et al.* Resonant addressing and manipulation of silicon vacancy qubits in silicon carbide. *Phys. Rev. Lett.* **109**, 226402 (2012).
6. Muller, T. *et al.* Optical signatures of silicon-vacancy spins in diamond. *Nat. Commun.* **5**, 3328 (2014).
7. Rogers, L. J. *et al.* All-optical initialization, readout, and coherent preparation of single silicon-vacancy spins in diamond. *Phys. Rev. Lett.* **113**, 263602 (2014).
8. Christle, D. J. *et al.* Isolated electron spins in silicon carbide with millisecond coherence times. *Nat. Mater.* **14**, 160–163 (2015).
9. Widmann, M. *et al.* Coherent control of single spins in silicon carbide at room temperature. *Nat. Mater.* **14**, 164–168 (2015).
10. von Bardeleben, H. J., Cantin, J. L., Rauls, E. & Gerstmann, U. Identification and magneto-optical properties of the NV center in 4H-SiC. *Phys. Rev. B* **92**, 064104 (2015).
11. Iwasaki, T. *et al.* Germanium-vacancy single color centers in diamond. *Sci. Rep.* **5**, 12882 (2015).
12. Barrett, S. D. & Kok, P. Efficient high-fidelity quantum computation using matter qubits and linear optics. *Phys. Rev. A* **71**, 060310 (2005).
13. Benjamin, S. C., Lovett, B. W. & Smith, J. M. Prospects for measurement-based quantum computing using solid state spins. *Laser Photon. Rev.* **3**, 556–574 (2009).
14. Batalov, A. *et al.* Temporal coherence of photons emitted by single nitrogen-vacancy defect centers in diamond using optical Rabi oscillations. *Phys. Rev. Lett.* **100**, 077401 (2008).
15. Togan, E. *et al.* Quantum entanglement between an optical photon and a solid-state spin qubit. *Nature* **466**, 730–734 (2010).
16. Hensen, B. *et al.* Loophole-free Bell inequality violation using electron spins separated by 1.3 kilometres. *Nature* **526**, 682–686 (2015).
17. Englund, D. *et al.* Deterministic coupling of a single nitrogen vacancy center to a photonic crystal cavity. *Nano Lett.* **10**, 3922–3926 (2010).
18. Faraon, A., Barclay, P. E., Santori, C., Fu, K.-M. C. & Beausoleil, R. G. Resonant enhancement of the zero-phonon emission from a colour centre in a diamond cavity. *Nat. Photon.* **5**, 301–305 (2011).
19. Riedrich-Möller, J. *et al.* One- and two-dimensional photonic crystal microcavities in single crystal diamond. *Nat. Nanotech.* **7**, 69–74 (2012).
20. Toyli, D. M. *et al.* Chip-scale nanofabrication of single spins and spin arrays in diamond. *Nano Lett.* **10**, 3168–3172 (2010).
21. Chu, Y. *et al.* Coherent optical transitions in implanted nitrogen vacancy centers. *Nano Lett.* **14**, 1982–1986 (2014).
22. McLellan, C. A. *et al.* Patterned formation of highly coherent nitrogen-vacancy centers using a focused electron irradiation technique. *Nano Lett.* **16**, 2450–2454 (2016).
23. Simmonds, R. D., Salter, P. S., Jesacher, A. & Booth, M. J. Three dimensional laser microfabrication in diamond using a dual adaptive optics system. *Opt. Express* **19**, 24122–24128 (2011).
24. Lagomarsino, S. *et al.* Photoionization of monocrystalline CVD diamond irradiated with ultrashort intense laser pulse. *Phys. Rev. B* **93**, 085128 (2016).
25. Yamamoto, T. *et al.* Extending spin coherence times of diamond qubits by high-temperature annealing. *Phys. Rev. B* **88**, 075206 (2013).
26. Uzan-Sagiv, C. *et al.* Damage threshold for ion-beam induced graphitization of diamond. *Appl. Phys. Lett.* **67**, 1194–1196 (1995).
27. Siyushev, P. *et al.* Optically controlled switching of the charge state of a single nitrogen-vacancy center in diamond at cryogenic temperatures. *Phys. Rev. Lett.* **110**, 167402 (2013).
28. Acosta, V. M. *et al.* Dynamic stabilization of the optical resonances of single nitrogen-vacancy centers in diamond. *Phys. Rev. Lett.* **108**, 206401 (2012).
29. Rondin, L. *et al.* Magnetometry with nitrogen-vacancy defects in diamond. *Rep. Prog. Phys.* **77**, 056503 (2014).
30. Ohno, K. *et al.* Engineering shallow spins in diamond with nitrogen delta-doping. *Appl. Phys. Lett.* **101**, 082413 (2012).
31. Pham, L. M. *et al.* Magnetic field imaging with nitrogen-vacancy ensembles. *New J. Phys.* **13**, 045021 (2011).
32. Courvoisier, A., Booth, M. J. & Salter, P. S. Inscription of 3D waveguides in diamond using an ultrafast laser. *Appl. Phys. Lett.* **109**, 031109 (2016).
33. Sotillo, B. *et al.* Diamond photonics platform enabled by femtosecond laser writing. *Sci. Rep.* **6**, 35566 (2016).
34. Kononenko, T. V. *et al.* Femtosecond laser microstructuring in the bulk of diamond. *Diam. Relat. Mater.* **18**, 196–199 (2009).

Acknowledgements

Y.-C.C. thanks DeBeers for financial support and S.N.I. acknowledges support from the EPSRC Centre for Doctoral Training in Diamond Science and Technology (EP/L015315/1). The work was supported by grants from the European Commission (Wavelength tunable Advanced Single Photon Sources (WASPS), grant agreement no 618078), the UK Engineering and Physical Sciences Research Council, (EP/M013243/1) and The Leverhulme Trust.

Author contributions

Y.-C.C. carried out the PL, HBT and PLE measurements with assistance from L.W., P.R.D., and S.J. and coordinated the work. P.S.S. performed the laser writing. S.K. performed the Hahn echo experiments with supervision from J.G.R. A.C.F., C.J.S., B.L.G. and S.N.I. annealed the samples and performed birefringence and Raman imaging with supervision from G.W.M. and M.E.N. J.M.S., M.J.B. and P.S.S. conceived and oversaw the project. All coauthors contributed to writing the manuscript.

Additional information

Supplementary information is available in the [online version of the paper](#). Reprints and permissions information is available online at www.nature.com/reprints. Correspondence and requests for materials should be addressed to J.M.S.

Competing financial interests

The authors declare no competing financial interests.

Methods

Samples and processing. The samples used were ‘electronic grade’ single-crystal plates from Element Six Ltd, with (001) crystal orientation and a nitrogen concentration of <5 ppb. Laser writing of vacancies was performed using a regeneratively amplified Ti:Sapphire laser (Spectra Physics Solstice). The optical layout for the laser processing is shown in Supplementary Fig. 4a. The laser beam was expanded onto a liquid crystal phase-only spatial light modulator (SLM) (Hamamatsu X10468-02), which was imaged in a 4f configuration onto the back aperture of a $\times 60$ 1.4NA Olympus PlanApo oil immersion objective. The diamond sample was mounted on precision translation stages (Aerotech x-y: ABL10100; z: ANT95-3-V) providing 3D control. An LED illuminated transmission microscope provided visualization of the sample during processing. Before the objective the laser pulse was linearly polarized and had a duration that was measured to be 250 fs using an intensity autocorrelator (APE Pulsecheck). The pulse duration at focus will be slightly increased due to dispersion in the objective lens. To optimize the aberration correction, the phase pattern displayed on the SLM was adjusted to minimize the pulse energy needed to produce visible fluorescence at test processing positions of similar depth in the sample.

The resulting point spread function in the diamond was approximated to be a gaussian beam with a cylindrically symmetric intensity distribution

$$I(r, z) = I_0 \frac{1}{1 + \left(\frac{z}{z_R}\right)^2} e^{-(2r^2/w_z^2)}$$

where $w_z = w_0 \sqrt{1 + (z/z_R)^2}$ is the beam width at axial displacement z , w_0 is the beam waist and z_R is the Rayleigh range. On the basis of the numerical aperture of the objective lens, we estimate that $w_0 = 297$ nm and $z_R = 852$ nm. These correspond to a full width at half maximum (FWHM) in the radial and axial directions for the photon intensity of $d_1 = 350$ nm and $L_1 = 1,704$ nm respectively, corresponding to a focal volume of $(\pi/4)d_1^2L_1 = 0.16 \mu\text{m}^3$. Single pulse energies for vacancy generation at the desired sites were controlled using a rotatable half-wave plate in conjunction with a Glan-Laser polarizer and measured before the microscope objective lens. The full list of pulse energies is given in Supplementary Table 1.

Positioning and number of vacancies. The vacancies generated at low pulse energies are thought to result from multiphoton ionization (MPI) (see Supplementary Information), in which energy is delivered to the diamond material as a result of multi-photon absorption before electronic relaxation. The nonlinearity of the absorption process is expected to lead to vacancy generation within a region smaller than the focal volume determined by the field intensity $I(r, z)$. The distribution function for the absorption of y photons is $I'(r, z)$, and the corresponding radial and axial dimensions (FWHM) are given by $d_y = w_0 \sqrt{2 \ln 2/y}$ and $L_y = 2z_R \sqrt{2^{1/y} - 1}$. Assuming²⁴ that $y = 9$ results in estimates of $d_9 = 117$ nm and $L_9 = 482$ nm. The volume over which vacancies are generated is therefore estimated to be $(\pi/4)d_9^2L_9 = 5.2 \times 10^{-3} \mu\text{m}^3$.

The number of vacancies produced is estimated from the graphitization threshold, reported²⁷ as $1,022 \text{ cm}^{-3}$, which over the volume calculated above suggests that 5.2×10^7 vacancies were produced with the 36 nJ pulse energy. Assuming a nine-photon process then provides an estimate of 10^7 vacancies at the GRI visibility threshold and $\sim 10^5$ at the lowest pulse energies needed to produce NV centres.

Annealing. Annealing was carried out in a tube furnace (Elite Thermal Systems TSH16/50/180-2416). The diamonds were placed in an alumina boat and buried in a sacrificial diamond grit (Element Six Micron+). Before annealing, the furnace was purged with dry nitrogen boil-off to minimize oxidation and graphitization of the diamond surface. Annealing was then carried out for 3 h at 1,000 °C, a temperature that is known to allow healing of the diamond lattice through removal of most of the extended lattice defects²⁶. Details of the optimization of the annealing process are provided in the Supplementary Information.

During the annealing, vacancies are assumed to diffuse isotropically following the 3D diffusion equation and bind with substitutional nitrogen atoms distributed randomly in the lattice to form stable NV colour centres. To facilitate comparison between the measured radial distribution of NV centres and a simple model, we assume that the initial vacancy distribution is elongated to an infinite extent in z , whereby the resulting distribution of NV centres relative to the focal position after an anneal time t will be

$$n_{\text{NV}}(r) = A r e^{-r^2/4Dt}$$

where A is a constant and D is the diffusivity. This approach neglects ‘end effects’ of the initial vacancy distribution but provides a good first approximation with which to analyse the positioning data.

PL and NV position measurements. PL imaging was carried out using a home-made scanning confocal microscope and spectroscopy with a 500mm spectrograph (Acton SpectraPro 500i) fitted with a back-illuminated CCD camera (Princeton Spec-10 100B), with >90% quantum efficiency across the wavelength range of interest. Excitation was performed using a frequency-doubled YAG laser ($\lambda = 532$ nm) with a maximum power delivery to the sample of 4 mW. A laser clean-up filter is used in excitation, combined with a 540 nm dichroic beam splitter and a 532 nm blocking notch filter in the collection optics. When recording a PL image, a 650 nm long-pass filter is inserted in the fluorescence collection path to block the diamond Raman emissions (all filters were from Semrock).

The position in the image plane of each NV centre was determined from the PL images by fitting a 2D Gaussian surface to the measured intensity distribution. The spatial resolution of the microscope (~500 nm) combined with the intensity of the single NV fluorescence images (~10,000 counts) allows Gaussian fitting with a standard error in the position of the NV centres of between 50 and 100 nm. After subtracting a quadratic field distortion for the PL microscope, determined using a PL image measured pre-anneal, these positions were compared with the uniform grid pattern locations targeted in the processing microscope (see Supplementary Information for supporting data).

Photoluminescence excitation (PLE) measurements. For PLE measurements the sample was cooled to 4.2 K in a liquid helium bath cryostat. An external cavity diode laser (Toptica DL100) was scanned through resonance with the NV ZPL at a wavelength of 637 nm, and the wavelength measured directly using a wavemeter (High Finesse WSU-30). No microwave modulation was applied, so the spin population time of the NV centres is very long and only the highly cycling upper branch $m_s = 0$ transition is observed.

Repump pulses were delivered from a frequency doubled diode-pumped solid state laser at 532 nm (CNI MGL-III-532), gated into 200 ms pulses using an acousto-optic modulator.

Photon autocorrelation measurements and data fitting. The photon autocorrelation function is defined by

$$g^{(2)}(\delta t) = \frac{\langle I(t)I(t + \delta t) \rangle}{\langle I(t) \rangle^2}$$

where $I(t)$ is the fluorescence intensity at time t .

Photon autocorrelation datasets were measured using the Hanbury Brown and Twiss method, using continuous wave 532 nm excitation at a power of 0.74 mW. The fluorescence was spectrally filtered using a 650 nm long-pass filter. To establish the statistics for $g^{(2)}(0)$ in Fig. 2 the results were fitted by the standard function for the photon autocorrelation of a three-level system derived using coupled rate equations:

$$g^{(2)}(\delta t) = g^{(2)}(0) + 1 - c \exp\left(\frac{-|\delta t|}{\tau_2}\right) + (c - 1) \exp\left(\frac{-|\delta t|}{\tau_3}\right)$$

where c , τ_2 and τ_3 are related to the interlevel rate constants, and $g^{(2)}(0)$ is a fixed background. No background correction was applied to the data before fitting. The solid red line in Fig. 2a is a least-squares fit of this equation to the measured data.

Hahn echo measurements. Hahn echo measurements ($\pi/2 - \tau_0 - \pi - \tau_1 - \text{echo}$, see Supplementary Fig. 8) were carried out on seven NV[−] centres. For each measurement, an external magnetic field of 6.7 mT was applied and carefully aligned parallel to the NV[−] centre axis. The splitting between the -1 and $+1$ fine transitions was large enough to ensure the individual driving of the -1 transition. The amplitude of the fluorescent echo signal was measured as a function of the pulse separation. The time duration of the $\pi/2$ pulse was chosen to be 20 ns (40 ns for a π pulse), determined by Rabi oscillation measurements on the $0 \leftrightarrow -1$ transition. Therefore the bandwidth was larger than the splitting, allowing full excitation of the $0 \leftrightarrow -1$ transition. A single Hahn echo measurement, that is, the iteration of τ_1 around the set value of τ_2 , consisted of a few million iterations of the pulse sequence and corresponds to about 3,500 photon detection events. The signal was normalized to the equilibrium between the -1 and 0 state of the optical pulse. The Hahn echo decay was measured over the first decay and on the revival.

Data availability. Original data can be accessed at <http://dx.doi.org/10.5287/bodleian:1aX8KOpwz>.